Chaos

Multiscale measures of phase-space trajectories

Cite as: Chaos **30**, 123116 (2020); https://doi.org/10.1063/5.0008916
Submitted: 26 March 2020 . Accepted: 12 November 2020 . Published Online: 03 December 2020

Tommaso Alberti, Giuseppe Consolini, Peter D. Ditlevsen, Reik V. Donner, and Virgilio Quattrociocchi

Multiscale measures of phase-space trajectories

Cite as: Chaos **30**, 123116 (2020); doi: 10.1063/5.0008916
Submitted: 26 March 2020 · Accepted: 12 November 2020 ·
Published Online: 3 December 2020

Tommaso Alberti,[1,a] Giuseppe Consolini,[1,b] Peter D. Ditlevsen,[2,c] Reik V. Donner,[3,4,d] and Virgilio Quattrociocchi[1,5,e]

AFFILIATIONS

[1]INAF-Istituto di Astrofisica e Planetologia Spaziali, Via del Fosso del Cavaliere 100, I-00133 Roma, Italy
[2]Centre for Ice and Climate, Niels Bohr Institute, University of Copenhagen, Copenhagen 2200, Denmark
[3]Department of Water, Environment, Construction and Safety, Magdeburg-Stendal University of Applied Sciences, Breitscheidstraße 2, 39114 Magdeburg, Germany
[4]Potsdam Institute for Climate Impact Research (PIK)—Member of the Leibniz Association, Telegrafenberg A31, 14473 Potsdam, Germany
[5]Dip. Scienze Fisiche e Chimiche, Università degli Studi dell'Aquila, Via Vetoio, I-67100 L'Aquila, Italy

[a]**Author to whom correspondence should be addressed:** tommaso.alberti@inaf.it
[b]giuseppe.consolini@inaf.it
[c]pditlev@nbi.ku.dk
[d]reik.donner@h2.de
[e]virgilio.quattrociocchi@inaf.it

ABSTRACT

Characterizing the multiscale nature of fluctuations from nonlinear and nonstationary time series is one of the most intensively studied contemporary problems in nonlinear sciences. In this work, we address this problem by combining two established concepts—empirical mode decomposition (EMD) and generalized fractal dimensions—into a unified analysis framework. Specifically, we demonstrate that the intrinsic mode functions derived by EMD can be used as a source of local (in terms of scales) information about the properties of the phase-space trajectory of the system under study, allowing us to derive *multiscale measures* when looking at the behavior of the generalized fractal dimensions at different scales. This formalism is applied to three well-known low-dimensional deterministic dynamical systems (the Hénon map, the Lorenz '63 system, and the standard map), three realizations of fractional Brownian motion with different Hurst exponents, and two somewhat higher-dimensional deterministic dynamical systems (the Lorenz '96 model and the on–off intermittency model). These examples allow us to assess the performance of our formalism with respect to practically relevant aspects like additive noise, different initial conditions, the length of the time series under study, low- vs high-dimensional dynamics, and bursting effects. Finally, by taking advantage of two real-world systems whose multiscale features have been widely investigated (a marine stack record providing a proxy of the global ice volume variability of the past 5×10^6 years and the SYM-H geomagnetic index), we also illustrate the applicability of this formalism to real-world time series.

Natural phenomena often display a chaotic and unpredictable behavior, as exemplified by weather forecasting or airplane turbulence, in which the behavior looks stochastic but is not random. They are also commonly characterized by multiscale interactions between different components whose origin is usually investigated by searching for scaling laws and/or by investigating the nature of fluctuations at different scales, allowing us to characterize their fractal/multifractal nature. Furthermore, deterministic-chaotic dissipative dynamical systems are also characterized by invariant manifolds, bifurcations, as well as (strange) attractors in their phase-space, whose geometric and topological properties are a reflection of the dynamical regimes of the system. Here, we propose a new formalism for characterizing the multiscale nature of phase-space trajectories of chaotic systems by using generalized fractal dimensions in combination with a data-adaptive time series decomposition technique.

I. INTRODUCTION

Chaos is frequently encountered in many natural systems and phenomena such as weather and climate,[1,2] turbulent flows,[3,4] the

near-Earth electromagnetic environment,[5] and so on. These systems are characterized by scaling behaviors, which reveal an underlying driving and/or coupling mechanism,[6–8] often associated with a fractal structure.[9] A fractal, in addition to being nowhere differentiable, is generally characterized by self-similarity, fine structure at arbitrarily small scales, and global/local irregularity that is not easily described in terms of the Euclidean geometry.[9,10] Its complexity is typically quantified by the so-called fractal dimensions accounting for changing detail in a pattern with changing scale,[11–13] also allowing us to discriminate between fractals and multifractals.[14] Specifically, for a (mono)fractal, only one parameter (i.e., the Hausdorff dimension) completely describes its behavior under changes of scale; otherwise, for a multifractal, a hierarchy of dimensions is needed to fully characterize its scaling behavior.[11]

Mathematically, fractals are usually described based on the definition of a partition function $\Gamma_q(\ell)$ via the coarse-grained weight of an invariant measure defined in terms of the probability of finding a filled portion of the phase-space.[11,13,15] Indeed, if we define a positive measure μ over a support Ω, in the limit $\ell \to 0$ $\Gamma_q(\ell)$ has a power-law behavior as

$$\Gamma_q(\ell) = \int_\Omega \mu(B_x(\ell))^{q-1} d\mu(x) \sim \ell^{(q-1)D_q}, \tag{1}$$

where $B_x(\ell)$ is a box of size ℓ centered at x.[11] Equation (1) allows us to draw a link between the geometric properties of the phase-space trajectories of dynamical systems and the statistics of the scaling properties. Specifically, by means of Eq. (1), we derive that $\mu(B_\ell(x)) \sim \ell^{D_q}$, thus relating the generalized fractal dimensions to the correlation integrals of q-tuplets of points on the phase-space.[11,12] Moreover, it is worthwhile to remark that for low-order q, this can be easily related to some useful measures like the box-counting dimension D_0, a statistical measure of complexity, the information dimension D_1, an information measure for random vectors, and the correlation dimension D_2, a measure of the dimensionality of the system's trajectory in phase-space.[11] By means of this multifractal formalism, new insights have already been gained in different fields as dynamical systems,[12,13] turbulence and intermittency,[16–22] and far-from-equilibrium systems.[5,23,24]

Nowadays, in the era of *big data and machine learning*, one of the main challenges of data analysis is extracting and interpreting information from signals (e.g., Refs. [25–28]). Obtaining such quantitative knowledge is particularly difficult when multiscale nonlinear and nonstationary signals are investigated.[29] Such multiscale variability can arise via a multiplicity of different mechanisms, including different oscillatory modes arising due to the internal variability of different interdependent components (like atmosphere and ocean in the climate system[30]), metastable states or specific (intermittent) dynamical regimes that are episodically approached, or multiple alternating dynamical patterns (like oscillations about different unstable fixed points in two- or multi-scroll chaotic oscillators such as the Lorenz '63 attractor[31]). Along with these different mechanisms, the specific properties of the resulting multiscale variability can differ markedly, for example, between distinct peaks and a broad continuum of time scales with significant variability in the power spectral density.

A particular challenge for the analysis of multiscale dynamics arises when studying fluctuations with respect to the average evolution in a system subject to random forces or undergoing chaotic motion.[32] Indeed, fluctuations are able to change the dynamical behavior of a system, including its collective properties and underlying (unknown) driving mechanisms. This is, for example, the case for the Brownian motion where the nonlinear path of the suspended particles is attributed to fluctuations due to random collisions with molecules, being a manifestation of the atomic nature of the medium.[33,34] Another example is turbulence where turbulent eddies, from the viewpoint of Richardson,[35] create field fluctuations whose singularities significantly affect the local behavior of the fluid, being characterized by an unpredictable and chaotic behavior[4,36] due to the nonlinear coupling of eddies of different size.[3,4,35–37] Thus, a correct characterization of the phase-space properties and their statistical measures would require a deep investigation of multiscale fluctuations and their effects on the estimates of generalized fractal dimensions. This should in principle call for an initial identification of the different scale-dependent components, which contribute to the whole dynamics of a given physical system, followed by the quantitative characterization of scale-specific complexity.

Here, we propose a new formalism to investigate the multiscale geometrical and topological properties of physical systems based on the combination of two established techniques: empirical mode decomposition (EMD) and generalized fractal dimensions. We employ the EMD to deal with the problem of identifying fluctuations at different scales.[38] It allows us to completely remove a priori mathematical assumptions such as stationarity and linearity of the signals under investigation, since the procedure is completely adaptive and based on local features of the signal.[38] Then, having derived the embedded components at different mean scales, those are used as a source of local (in terms of scale) information. For this purpose, we introduce a new concept of *multiscale measures* by deriving the generalized fractal dimensions for each embedded structure. In this way, a new formalism, based on multiscale features of signals, is built up with the main aim of investigating how complexity varies among scales in a complex system, i.e., a physical system composed of many components which may interact with each other. The suitability of the above formalism is first illustrated for three paradigmatic deterministic model systems (the Lorenz '63 system, the Hénon map, and the standard map) as well as three realizations of fractional Brownian motion, a widely studied type of stochastic processes, with different values of the Hurst exponent. We further present the corresponding results obtained from the analysis of two somewhat higher-dimensional dynamical systems (the Lorenz '96 system and the on–off intermittency model). Finally, we discuss the application of our formalism to two real-world time series capturing the long-term behavior of the global climate during the last 5 million years (Myr)[39] and the dynamical properties of the near-Earth electromagnetic environment as monitored by the SYM-H index.[40]

II. METHODS

A. Empirical mode decomposition (EMD)

Empirical mode decomposition (EMD), first introduced by Huang *et al.*,[38] is an adaptive decomposition method for detecting oscillatory structures embedded within complex univariate signals.

Unlike considering a fixed decomposition basis in a mathematical space (as for Fourier and wavelet decompositions), the EMD procedure is based on an algorithmic procedure, known as the sifting process, which derives the decomposition basis by means of an iterative process exploiting the local properties of signals, with no a priori assumptions and requirements of linearity and/or stationarity of the analyzed signals.[38] For a given signal $s(t)$, the sifting process acts as follows:

(1) a zero-mean signal is constructed from $s(t)$, i.e., $r(t) = s(t) - \langle s(t)\rangle_t$, with $\langle\cdots\rangle_t$ denoting the time average;
(2) the local maxima and minima of $r(t)$ are identified and interpolated by using cubic splines to derive upper and lower envelopes;
(3) the mean $e_m(t)$ of the two envelopes is computed and subtracted from $r(t)$ to define a detail $h(t) = r(t) - e_m(t)$;
(4) if the numbers of extrema and zero crossings are equal or differs at most by one and if the mean envelope of $h(t)$ has a zero mean, then $h(t)$ is assigned to be an Intrinsic Mode Function (IMF) or empirical mode; otherwise steps 1–3 are iterated n times until a candidate detail $h_n(t)$ is assigned to be an IMF; and
(5) steps 1–4 are repeated on the residual $r_{h_n}(t) = r(t) - h_n(t)$ until no more IMFs can be extracted.

From an analytical point of view, an IMF can be found only when $n \to \infty$. Thus, from a numerical perspective, a stopping criterion is needed to avoid an infinite loop cycle.[38,41] Huang *et al.*[38] first proposed a Cauchy-type convergence criterion in which the sifting process is stopped when

$$\sigma_n = \sum_j \frac{|h_n(t_j) - h_{n+1}(t_j)|^2}{h_n(t_j)^2} < \epsilon, \tag{2}$$

typically with $\epsilon \in [0.2, 0.3]$. In 2003, Rilling *et al.*[42] suggested a new stopping criterion known as threshold method in which two thresholds, θ_1 and θ_2, are set to guarantee globally small fluctuations[38] along with allowing for locally large excursions.[41]

When the sifting process is completed, i.e., when no more IMFs can be extracted, the decomposition basis is formed by the set of IMFs $\{c_k(t)\}$, plus a residue of the decomposition $r(t)$, e.g., a non-oscillating function of time[38] commonly describing monotonic trends in the mean of the signal under study, such that

$$s(t) = \sum_{k=1}^{N_k} c_k(t) + r(t), \tag{3}$$

with N_k being the number of detected IMFs. Thus, it is a completely adaptive procedure, highly suitable for deriving embedded structures from nonlinear and/or nonstationary data.[43] Furthermore, the decomposition basis $\{c_k(t)\}$ satisfies all mathematical requirements of a basis in an $\mathbb{L}^2$ Hilbert space, including completeness, which is ensured by construction [see Eq. (3)], convergence, both analytically and numerically,[38,42] local orthogonality, being derived from the local properties of the zeros of the first derivative, while global orthogonality, unless not theoretically guaranteed, is a posteriori satisfied since $\langle c_i, c_j\rangle = \delta_{ij}$, with $\langle\cdot,\cdot\rangle$ and δ_{ij} being the inner product and the Kronecker tensor, respectively.

Once the decomposition has been completed, by means of the so-called Hilbert Transform (HT), we are able to investigate the local amplitude–frequency modulation embedded in a time series (e.g., Ref. 38). Given an empirical mode $c_k(t) \in \mathbb{L}^2$, its HT $\tilde{c}_k(t)$ can be defined as

$$\tilde{c}_k(t) = \frac{1}{\pi}\mathscr{P}\int_0^\infty \frac{c_k(t')}{t - t'}dt', \tag{4}$$

with $\mathscr{P}$ denoting the Cauchy principal value. By means of the conjugate pair $\{c_k(t), \tilde{c}_k(t)\}$, we can introduce a complex signal

$$z_k(t) = c_k(t) + i\,\tilde{c}_k(t) = a_k(t)e^{i\phi_k(t)}, \tag{5}$$

with

$$a_k(t) = \sqrt{c_k(t)^2 + \tilde{c}_k(t)^2}, \tag{6}$$

$$\phi_k(t) = \tan^{-1}\left[\frac{\tilde{c}_k(t)}{c_k(t)}\right], \tag{7}$$

where $a_k(t)$ and $\phi_k(t)$ are the instantaneous amplitude and phase of the kth empirical mode, respectively. Using the latter concept of instantaneous phase, the definition of an instantaneous frequency immediately follows as $\omega_k(t) = \frac{1}{2\pi}\frac{d\phi_k(t)}{dt}$ along with that of a mean timescale $\tau_k = \langle\omega_k^{-1}(t)\rangle_t$, with $\langle\cdots\rangle_t$ identifying the time average.

Furthermore, by the set of empirical modes $\{c_k(t)\}$, the frequency–time distribution of the amplitude can be derived by defining the so-called Hilbert–Huang spectrum $H(\omega, t) = a^2(\omega, t)$, e.g., by contouring the squared instantaneous amplitudes in a time–frequency plane.[38] It represents the original signal at the local level and can be used to define the joint probability density function $P(\omega, a)$ of finding a pair of values $\{\omega, a\}$ from the whole set of values of both the instantaneous frequencies $\omega_k(t)$ and amplitudes $a_k(t)$ of all IMFs together. Accordingly, the so-called Hilbert marginal spectrum can be derived as $H(\omega) = \int_0^\infty P(\omega, a)a^2 da$, which can be easily generalized to a given moment order $q \geq 0$ by defining $\mathscr{L}_q(\omega) = \int_0^\infty P(\omega, a)a^q da$, accounting for the statistical moment frequency distribution.[44]

B. Generalized fractal dimensions

Let $\{s_i\}_{i=1}^N$ be a signal whose trajectory belongs to a D-dimensional space $\mathscr{S}^D$, $D = 1, \ldots, \infty$, although typically lying on a subset $\mathscr{S}^d \subseteq \mathscr{S}^D$, with $d < D$. Assuming a partition of the D-dimensional space into M_i hypercubes of size ℓ_i, by defining $p_i \doteq \lim_{N\to\infty}(N_i/N)$ (with N_i denoting the number of data points falling into the ith hypercube) as the probability of visiting the ith box, a natural measure of the phase-space trajectory $d\mu(\{s_i\})$ can be defined since $p_i = \int_{i\in M_i} d\mu(\{s_i\})$.[13] By recalling Eq. (1) and letting $B_s(\ell)$ be the hypercube of size ℓ centered at the point s in this phase-space, Hentschel and Procaccia[11] derived

$$D_q = \frac{1}{q-1}\lim_{\ell\to 0}\frac{\log\Gamma_q(\mu, B_s(\ell))}{\log\ell} = \frac{1}{q-1}\lim_{\ell\to 0}\frac{\log\sum_i p_i^q}{\log\ell}. \tag{8}$$

From Eq. (8), it directly follows that

- $D_0 = -\lim_{\ell\to 0}\frac{\log N(\ell)}{\log\ell}$ is the fractal (or similarity, capacity, or box-counting) dimension, with $N(\ell)$ being the number of hypercubes of size ℓ containing points on the observed trajectory in phase-space;

- $D_1 = \lim_{q\to 1} \frac{1}{q-1} \lim_{\ell\to 0} \frac{\log \sum_i p_i}{\log \ell} = -\lim_{\ell\to 0} \frac{S(\ell)}{\log \ell}$ is the information dimension, with $S(\ell) = -\sum_i p_i \log p_i$ being the Shannon entropy;[25]
- $D_2 = \lim_{\ell\to 0} \frac{\log \sum_i p_i^2}{\log \ell} = \lim_{\ell\to 0} \frac{\log C(\ell)}{\log \ell}$ is the correlation dimension, with $C(\ell)$ being the correlation integral;[11,13] and
- $D_{q>2}$ are the generalized dimensions associated with the correlation integrals of q-tuplets of points in phase-space.[11]

C. Multiscale measures of fluctuations

As stated in Sec. I, many natural phenomena comprise multiscale fluctuations of different origin and with different dynamical properties, which contribute to the collective behavior of a physical system, although less attention has been paid so far to measuring information at different scales. To deal with this problem a new formalism is introduced below based on the combination of the previous concepts of empirical mode decomposition and generalized fractal dimensions. By keeping in mind that a signal could manifest a multiscale behavior and writing,

$$s(t) = \langle s \rangle + \sum_\tau \delta s_\tau(t), \tag{9}$$

with $\langle s \rangle$ being a steady-state average value and $\delta s_\tau(t)$ a fluctuation at scale τ; we can define, for $\sum_\tau \delta s_\tau(t)$, a local (in terms of time scale) natural measure $d\mu_\tau$, in a way similar to the concept of scale-local Rényi dimensions.[10,45,46] For this purpose, we first consider a partition function

$$\Gamma_q(\mu_\tau, B_{s,\tau}(\ell)) = \int d\mu_\tau(s) \mu_\tau(B_{s,\tau}(\ell))^q \underset{\ell\to 0}{\sim} \ell^{(q-1)D_{q,\tau}}, \tag{10}$$

with $B_{s,\tau}(\ell)$ being the hypercube of size ℓ centered at the point s on the space of the $\sum_\tau \delta s_\tau$. Thus, the multiscale generalized fractal dimensions read

$$D_{q,\tau} = \frac{1}{q-1} \lim_{\ell\to 0} \frac{\log \Gamma_q(\mu_\tau, B_{s,\tau}(\ell))}{\log \ell}. \tag{11}$$

This approach is quite similar to the concept of partial (or directional) dimensions proposed by Grassberger[47] allowing a decomposition of the phase-space trajectory into three main directions: continua, discrete points, and Cantor-like sets.[47] They are generalizations of the Hausdorff dimension derived from covering the phase-space by means of ellipsoids of different sizes, thus properly considering the phase-space coverage over different directions. However, instead of fixing a direction, here we deal with deriving the intrinsic scales embedded in the signal $s(t)$ by using an adaptive nonlinear and nonstationary procedure like the EMD (i.e., $\delta s_\tau(t) \equiv c_k(t)$) and then deriving information on the phase-space trajectory by investigating the behavior of the generalized dimensions at different scales τ. Thus, the procedure can be summarized by the following steps:

(1) extract embedded oscillations from $s(t)$ by using the EMD;
(2) evaluate the intrinsic mean timescale τ_k of each IMF (indexed by k);
(3) evaluate partial sums of Eq. (3) at different scales

$$\sum_\tau \delta s_\tau(t) \to F_{k^*}(t) = \sum_{k=1}^{k^*} c_k(t), \tag{12}$$

with $k^* = 1, \ldots, N_k$ (we remark that by construction, IMFs are ordered from short to long scales, e.g., $\tau_{k_1} < \tau_{k_2}$ if $k_1 < k_2$);
(4) for each scale k^* (i.e., for each τ_{k^*}) evaluate the multiscale generalized dimensions $D_{q,\tau}$ from $F_{k^*}(t)$; and
(5) by using the Legendre transform evaluate the multiscale singularities and singularity spectrum

$$\alpha_\tau = \frac{d}{dq}\left[(q-1)D_{q,\tau}\right], \tag{13}$$

$$f_\tau = f(\alpha_\tau) = q\alpha_\tau - \left[(q-1)D_{q,\tau}\right]. \tag{14}$$

From Eq. (12), we may expect that when $k^* \to N_k$, then $D_{q,\tau} \to D_q$, with D_q being the generalized fractal dimensions proposed by Hentschel and Procaccia.[11] Notably, the dynamical behavior of a multiscale nonlinear and nonstationary system is strongly affected by the local properties of fluctuations such that different dynamical features and behaviors can be investigated by following this approach. In the following, we provide some illustrative numerical examples and highlight possible applications to real-world systems to disentangle the different dynamical components and characterize processes of different origin.

III. NUMERICAL EXAMPLES

A. A low-dimensional discrete system: The Hénon map

As a first example, we consider the Hénon map,[48] a time-discrete dissipative deterministic dynamical system defined as

$$x_{t+1} = 1 - \mu_1 x_t^2 + y_t, \tag{15}$$

$$y_{t+1} = \mu_2 x_t, \tag{16}$$

with μ_1 and μ_2 being two control parameters. Originally introduced as a simplified model of the Poincaré section of the famous Lorenz '63 system (see below), it exhibits chaotic behavior with a strange attractor when $\mu_1 = 1.4$ and $\mu_2 = 0.3$ as shown in Fig. 1 (left panel, black dots), and a fractal nature, smooth in one direction and a Cantor set in the other, leading to $D_0 \simeq D_1 \simeq D_2 = 1.24 \pm 0.03$, accounting for small discrepancies with generally $\{D_0, D_1, D_2\} \in [1.21, 1.26]$.[12] Being further characterized by a broad power spectrum with (depending on the control parameter values) several possible peaks,[49] we consider the Hénon system as an example for a dynamical system exhibiting variability at multiple scales.

We numerically solve the Hénon map by using a total number of $N = 8192$ iterations and apply the EMD algorithm to the resulting time series of both x_t and y_t separately (for comparison, we also evaluated IMFs obtained only for x_t, since y_t is immediately derived from x_t, and we could confirm that the empirical modes extracted from y_t are the same than those extracted from bx_t). We obtain a set of $N_k = 11$ empirical modes for both dynamical variables x_t and y_t, with timescales ranging between $\tau_1 \approx 3$ a.u. (arbitrary units) and $\tau_{11} \approx 3000$ a.u. Then, we evaluate (without

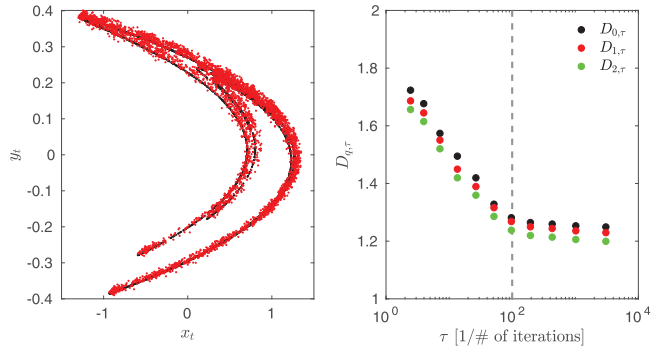

FIG. 1. Left: Phase-space portrait of the Hénon map based on the raw time series (black) and empirical mode reconstructions (red) using partial sums of Eq. (12) up to $k^* = 7$. Right: Behavior of the multiscale generalized fractal dimensions $D_{q,\tau}$ in dependence on the timescale τ. The gray dashed line marks the timescale τ^* at which the multiscale generalized dimensions $D_{q,\tau}$ converge to the expected fractal dimensions D_q.

considering time-delay embedding as in Takens[50]) the multiscale generalized dimensions $D_{q,\tau}$ for different k^* whose behavior as a function of τ is reported in the right panel of Fig. 1. We clearly note a timescale dependence of the generalized fractal dimensions, with $D_{q,\tau}$ decreasing as the timescale τ increases, converging toward the expected value of $D_q = 1.24 \pm 0.03$. The expected value is obtained for $k^* = 7 < N_k = 11$, thus suggesting that a subset of modes contains the essential information of the time series. Therefore, we can consider reconstructions of IMFs up to the mode index at which $D_{q,\tau}$ approaches a constant (i.e., the expected value D_q),

$$F^{(x)}_{7,t} = x^*_t = \sum_{k=1}^{7} c^{(x)}_{k,t}, \tag{17}$$

$$F^{(y)}_{7,t} = y^*_t = \sum_{k=1}^{7} c^{(y)}_{k,t}, \tag{18}$$

and investigate the phase-space dynamics in the 2D phase-space (x^*_t, y^*_t) as reported in the left panel of Fig. 1 (red points). By comparing the phase-space dynamics obtained by using the whole time series x_t and y_t with that obtained by x^*_t and y^*_t, a pretty good agreement is found, thus confirming that the whole information about the geometric and topological properties of the Hénon map is stored in a subset of "informative" empirical modes.

We further use the Hénon system to assess the performance of our formalism with respect to noise, sensitivity to the initial conditions, and to the number of iterations (length of the time series). These are crucial aspects for the estimation of generalized fractal dimensions as emphasized in Ref. 11. We only show here the results for $q = 2$ for a better comparison between the different cases; however, similar considerations can be drawn also for $q \neq 2$ (not shown).

As expected, there is an effect due to the length of the time series (see Fig. 2, left panel), especially for the short-timescale modes. This feature had already been reported in the seminal work by Hentschel and Procaccia[11], who first stated that there should be a

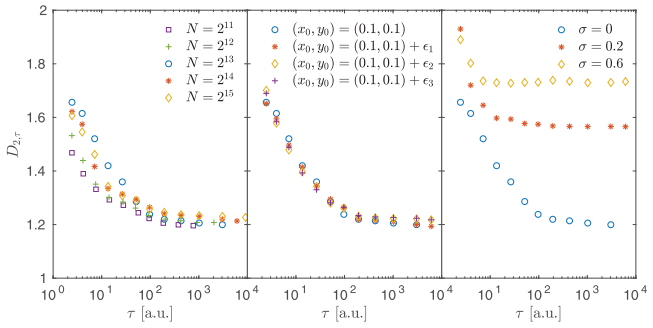

FIG. 2. Behavior of the multiscale generalized fractal dimension $D_{2,\tau}$ for the Hénon map in dependence on the timescale τ for different number of iterations N (left panel), different initial conditions (middle panel, $N = 2^{13}$, $\epsilon_i < \epsilon = 0.01$ for $i = 1, 2, 3$), and different noise levels σ (right panel, $N = 2^{13}$).

sufficient number of points to accurately estimate the generalized fractal dimensions. However, the value at which $D_{2,\tau}$ converges for the different numbers of data points is compatible with the estimate of $D_2 \simeq 1.22 \pm 0.03$ for the Hénon system,[11] and the timescale τ_{k*} at which the convergence is first observed does not change with the number of points ($\tau_{k^*} \sim 200$ a.u. for $N = 2^{13}, 2^{14}, 2^{15}$). Moreover, we also assess the significance of our multiscale dimension estimates with respect to the initial condition of the Hénon map. To deal with this aspect, we study four different realizations of the Hénon system (without noise) starting from initial conditions within a circle of radius $\epsilon = 0.01$ around the point $(x_0, y_0) = (0.1, 0.1)$. As shown in the central panel of Fig. 2, there is no significant dependence of our results on the choice of the initial condition.[51] As a final test, we also show that the generalized fractal dimension increases (as expected) when Gaussian white noise is added to the Hénon map (see Fig. 2, right panel), leading to markedly elevated correlation dimension estimates.[52] It is notable that the particularly large correlation dimension estimates close to $D_2 = 2$ that are associated with the first IMF are compatible with the expected value for white noise (see below), which supports the previously reported feature of the EMD to extract the noise component of time series as its first empirical mode.[38,53]

These latter results are further confirmed by looking at the behavior of the multiscale generalized fractal dimensions $D_{q,\tau}$ for a purely white Gaussian noise process as reported in Fig. 3. We clearly note a scale-independent nature of $D_{q,\tau}$, immediately converging to the expected value $D_q = D_0 = 2 \quad \forall q > 0$ when only the first empirical mode is considered with an embedding dimension $m = 2$ corresponding to the number of variables of the Hénon map. This result thereby highlights the mono-fractal nature of white noise processes at all timescales[9] and allows us to directly assess the performance of our formalism with respect to a white noise. We also estimated the multiscale generalized fractal dimensions for different colored Gaussian noise realizations with various Hurst exponents H. For all those cases, we consistently obtained a scale-independent nature of $D_{q,\tau}$ that converge toward the expected value of $D_q = D_0 = 2 - H \quad \forall q > 0$ (not shown). We also observed that, as expected,[53] for all realizations, the EMD is able to extract the same number of IMFs that corresponds to $\log_2 N = 13$.

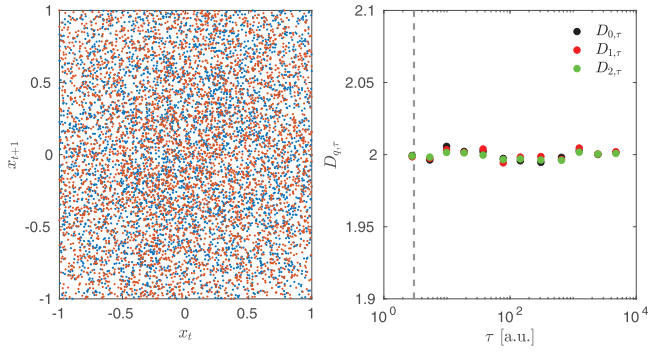

FIG. 3. Left: Phase-space portrait of a pure white noise ($N = 2^{13}$) as obtained from the raw time series (blue) and empirical mode reconstructions (orange) by using partial sums of Eq. (12). Right: Behavior of the multiscale generalized fractal dimensions $D_{q,\tau}$ in dependence on the timescale τ. The gray dashed line marks the timescale τ^* at which the multiscale generalized dimensions $D_{q,\tau}$ converge to the expected fractal dimensions D_q.

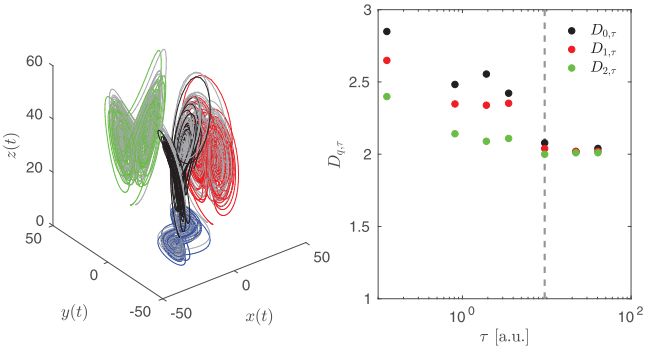

FIG. 4. Left: Phase-space portrait of the Lorenz '63 system based on the raw time series (gray lines) and empirical mode reconstructions (colored lines) by using partial sums of Eq. (12) up to $k^* = 5$. Right: Behavior of the multiscale generalized fractal dimensions $D_{q,\tau}$ in dependence on the timescale τ. The gray dashed line marks the timescale τ^* at which the multiscale generalized dimensions $D_{q,\tau}$ converge to the expected fractal dimensions D_q.

B. A low-dimensional continuous flow: The Lorenz '63 system

As a second example, we show the results of our formalism in deriving the multiscale generalized fractal dimensions of the Lorenz '63 system.[31] It is defined by the following set of three coupled ordinary differential equations,

$$\dot{x} = -\sigma(x - y), \tag{19}$$

$$\dot{y} = rx - y - xz, \tag{20}$$

$$\dot{z} = xy - bz, \tag{21}$$

manifesting a chaotic behavior with a well-known strange attractor, as illustrated in Fig. 4 for $(\sigma, r, b) = (10, 28, 8/3)$. The behavior of the Lorenz '63 system has been thoroughly investigated elsewhere, also concerning the characterization of the dimensionality of its phase-space trajectories for which $D_q = 2.05 \pm 0.02\ \forall q > 0$ (e.g., 11 and 12). Its multiscale dynamics originates from the presence of two distinct processes—chaotic oscillations in any of the two parts of the associated double-scroll attractor and jumps between both parts—along with the presence of weakly repulsive unstable low-periodic orbits and leads to a broad power spectrum with eventually arising spectral peaks.[54]

Here, we use Euler's method to generate a numerical solution of Eqs. (19)–(21) with a time step of $\Delta t = 10^{-2}$ a.u., a total number of iterations $N = 8192$, and random initial conditions for the three dynamical variables $(x(t_0), y(t_0), z(t_0)) = (x_0, y_0, z_0)$. As usual for dissipative dynamical systems, we start from some initial transient before the attractor is reached, which is then eliminated by removing the first part of the trajectory. We separately decomposed each dynamical variable (i.e., x, y, and z) via the EMD (we also decomposed all dynamical variables via a multivariate extension of the EMD (i.e., the MEMD algorithm[82]) and we derived the same number of empirical modes with similar dynamical features) and thereby derived a set of $N_k = 7$ empirical modes for each dynamical variable, with timescales ranging from $\tau_1 \approx 0.1$ a.u. to $\tau_7 \approx 40$ a.u. It is interesting to note that the first empirical mode oscillates with a mean timescale which is compatible with the characteristic frequency of the Lorenz '63 system for $(\sigma, r, b) = (10, 28, 8/3)$, which has been found to be $\omega_0 \sim 8.3$.[55,56] Then, we evaluate $F_{k^*}(t)$ as in Eq. (12) for $k^* \in [1, N_k]$ and the multiscale generalized fractal dimensions $D_{q,\tau}$ as in Eq. (11). The behavior of $D_{q,\tau}$ as a function of the mean timescale τ of each empirical mode, derived without using time-delay embedding technique but directly exploring the phase-space of the Lorenz '63 system,[50] is reported in Fig. 4.

From Fig. 4, we note that the values of the generalized fractal dimensions $D_{q,\tau}$ exhibit a clear timescale dependence, decreasing as the timescale increases, as a consequence of the "more regular" and smoother behavior of empirical modes moving from short to long timescales, approaching the expected value of $D_q = 2.05$[12] when $k^* = 5$, which is again less than the total number of IMFs carried out by the procedure ($N_k = 7$). As previously stated, due to the completeness property of the EMD following from Eq. (3), we clearly expect that when $k^* \to N_k$, then $D_{q,\tau} \to D_q$ with D_q being the generalized fractal dimensions as proposed by Hentschel and Procaccia.[11] However, here we note again that the expected dimensions are approached when $k^* < N_k$, i.e., that only a subset of empirical modes is needed to recover the essential geometric and topological information on the phase-space of the Lorenz '63 system. Thus, by keeping fixed $k^* = 5$, we reconstruct $F_{k^*}(t) = F_5(t)$ as in Eq. (12) for each dynamical variable as

$$F_5^{(x)}(t) = x^*(t) = \sum_{k=1}^{5} c_k^{(x)}(t), \tag{22}$$

$$F_5^{(y)}(t) = y^*(t) = \sum_{k=1}^{5} c_k^{(y)}(t), \tag{23}$$

$$F_5^{(z)}(t) = z^*(t) = \sum_{k=1}^{5} c_k^{(z)}(t), \tag{24}$$

and investigate the phase-space dynamics in the 3D phase-space (x^*, y^*, z^*) as reported in Fig. 4 (colored lines). It is clearly notable that the geometric properties of the Lorenz '63 attractor are recovered, thus suggesting that we can infer both geometric and topological information about the phase-space trajectories with few "informative" empirical modes, i.e., a reduction in the complexity has been obtained, together with a clear scale-to-scale dependence of geometric and topological properties of the Lorenz '63 system.

C. A low-dimensional multifractal discrete system: The standard map

As a third low-dimensional deterministic example, we consider the (non-dissipative) standard map defined as

$$p_{t+1} = p_t - K \sin(2\pi\theta_t), \tag{25}$$

$$\theta_{t+1} = \theta_t + p_{t+1}, \tag{26}$$

with fixed $K = 1$, which marks the onset value of a chaotic behavior that can be well recognized in the (θ_t, θ_{t+1}) plane (see Fig. 5, left panel). When the standard map is considered, a wider spectrum of generalized dimensions is found (e.g., Ref. 13), some of which can be analytically evaluated by means of a similarity with the Fibonacci numbers, leading us to have a bounded region for $D_q \in [D_\infty, D_{-\infty}] = [0.5, 0.924]$[13] and $D_0 \simeq 0.87$.[57] This provides evidence for a multifractal nature of the standard map, which is the reason why we consider this map as a last low-dimensional deterministic example in order to test if our formalism could be also helpful for distinguishing between monofractals and multifractals. As the two previously discussed low-dimensional deterministic systems, the standard map also exhibits multiscale dynamics[58] associated with the presence of a mixed phase-space with regular and chaotic domains leading to the stickiness phenomenon, i.e., intermittent trapping of chaotic trajectories in the vicinity of regular islands.[59,60]

After having numerically iterated the standard map up to $N = 8192$ with initial conditions in the domain of Hamiltonian chaos, we apply the EMD procedure carrying out a set of $N_k = 11$ empirical modes, whose timescales range between $\tau_1 \approx 4$ a.u. and $\tau_{11} \approx 2800$ a.u. Then, we evaluate the multiscale generalized fractal dimensions $D_{q,\tau}$ at different timescales τ and we clearly note that (i) $D_{q,\tau}$ approaches the expected dimensions D_q when $k^* \to N_k$, and (ii) multifractal features emerge, with $D_{q,\tau} \neq D_{q',\tau}$ when $q \neq q'$, as reported in the right panel of Fig. 6. However, as for both the Lorenz '63 system and the Hénon map, the expected dimensions D_q are recovered with a subset of empirical modes, here $k^* = 6 < N_k$, and the geometry of the trajectory in phase-space can be reproduced by considering partial sums of Eq. (12)

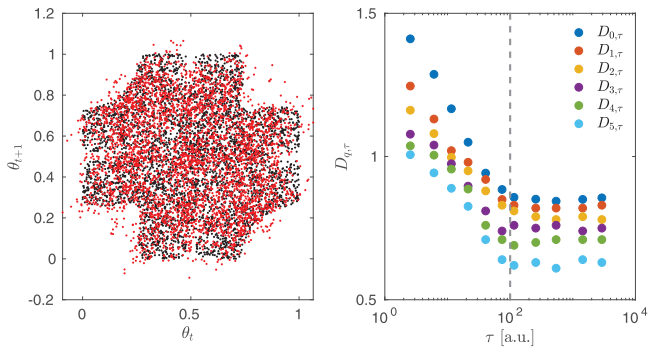

FIG. 5. Left: Phase-space portrait of the standard map as obtained from the raw time series (θ_t, θ_{t+1}) (black) and from reconstructions of empirical modes $(\theta_t^*, \theta_{t+1}^*)$ up to $k^* = 6$ (red). Right: Behavior of the multiscale generalized fractal dimensions $D_{q,\tau}$ vs the timescale τ for $q \in [0, 5]$. The gray dashed line marks the timescale τ^* at which the multiscale generalized dimensions $D_{q,\tau}$ converge to the fractal dimensions D_q.

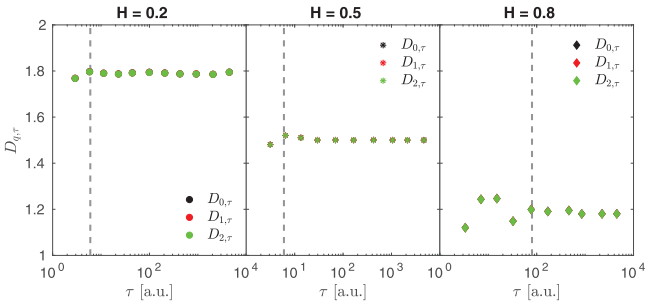

FIG. 6. The behavior of the multiscale generalized fractal dimensions $D_{q,\tau}$ in dependence on the timescale τ for the three different fBm realizations each consisting of $N = 2^{13}$ points. The gray dashed lines mark the timescales τ^* at which the multiscale generalized dimensions $D_{q,\tau}$ converge to the expected fractal dimensions $D_q = 2 - H\ \forall q > 0$, supporting the mono-fractal character of fBm.

$$F_{6,t}^{(\theta)} = \theta_t^* = \sum_{k=1}^{6} c_k^{(\theta_t)}, \tag{27}$$

$$F_{6,t}^{(p)} = p_t^* = \sum_{k=1}^{6} c_k^{(p_t)}, \tag{28}$$

thus allowing to again derive the essential geometric and topological information by using only few empirical modes (see Fig. 5, red points) as well as to show that the multifractal nature is a feature of the different timescales.

D. A one-dimensional stochastic process: The fractional Brownian motion

In order to complement the results for the previously mentioned case of white Gaussian noise, we next discuss the application of our formalism to three different stochastic processes belonging to the class of fractional Brownian motion. Fractional Brownian motion (fBm) provides a simple stochastic process model in statistics and information theory that accounts for the observational evidence of power-law spectra in natural time series.[9] It can be completely described by a single parameter, the Hurst exponent H, which quantifies the associated degree of long-range dependence of the process. Due to its monofractal nature, its self-similarity property, and its Gaussian distribution, fBm is characterized by $D_q = D_0 = 2 - H\ \ \forall q > 0$.[9] Here, we consider three different

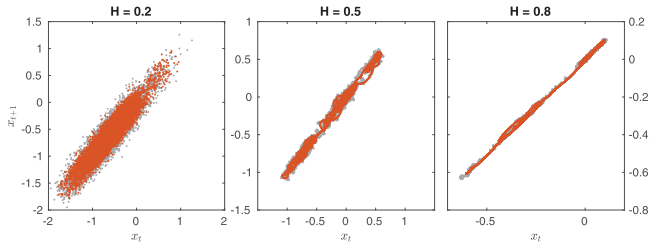

FIG. 7. Phase-space portraits of three realizations of fractional Brownian motion with Hurst exponents $H = 0.2$, 0.5, and 0.8 (left to right) as obtained from the raw time series $[(x_t, x_{t+1})$, gray] and from reconstructions of empirical modes $[(x^*_t, x^*_{t+1})$, orange].

choices of H, corresponding to an anti-persistent ($H = 0.2$), a classical Brownian motion ($H = 0.5$), and a persistent case ($H = 0.8$), respectively.

By looking at the multiscale generalized fractal dimensions $D_{q,\tau}$ (Fig. 6), we are able to detect a scale-independent behavior with $D_{q,\tau} \to 2 - H$ within the first two empirical modes for the cases $H = 0.2$ and $H = 0.5$, while the expected fractal dimensions are recovered at $k^* = 5$ for $H = 0.8$. This behavior of the multiscale generalized fractal dimensions can be easily understood in terms of the different dynamical properties of fBm as the Hurst exponent approaches values larger than 0.5. Indeed, a more regular behavior is observed for $H > 0.5$ with a long-range correlated nature whose dynamical features are embedded in long-timescale empirical modes; conversely, for $H < 0.5$, the dynamics is well captured by short-term empirical modes; thus, $D_{q,\tau}$ tend to converge soon to the expected values.[9] Moreover, all D_q for $q = 0$, 1, and 2 collapse to the same values for the different τ values, supporting the mono-fractal character of fractional Brownian motion.[9]

These aforementioned features are easily observed by considering reconstructions of IMFs up to the mode index at which $D_{q,\tau}$ approaches a constant value (i.e., the expected value D_q) and by comparing the phase-space dynamics obtained by using the whole time series with that obtained by the reconstruction based on IMFs. Indeed, a pretty good agreement is found (see Fig. 7), thus confirming that the essential information about the geometric and topological properties is again stored in a subset of "informative" empirical modes.

E. A higher-dimensional system: The Lorenz '96 model

By means of the previous deterministic examples, we were able to assess the performance of our formalism when applied to low-dimensional systems that can be seen as idealized low-order reductions of some more complex real-world systems. We now discuss the corresponding results for a higher-dimensional deterministic dynamical system, the Lorenz '96 model.[61] It is a simple system that Lorenz developed to bring the attention to the concept of "predictability" in weather forecasting[62] in which the model variables are representative of the continuous time variation of an atmospheric quantity of interest at specific (discrete) locations on a periodic lattice representing a latitude circle.[61] Despite its simplicity and phenomenological derivation, it is considered one of the main

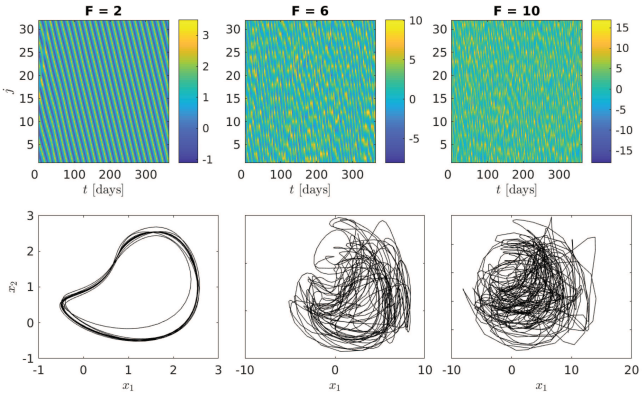

FIG. 8. Top: Contours for a subset of time points corresponding to 1 year of the Lorenz '96 model for three different values of the constant external forcing: (upper left) $F = 2$, (upper middle) $F = 6$, and (upper right) $F = 10$. Bottom: Phase-space portraits of the first two variables (x_1, x_2) for the three different cases: (lower left) $F = 2$, (lower middle) $F = 6$, and (lower right) $F = 10$.

examples for studying the route toward spatiotemporal chaos.[63] The model reads as

$$\dot{x}_j = (x_{j+1} - x_{j-2})x_{j-1} - x_j + F, \tag{29}$$

where $j = 1, \ldots, N_v$, x_j is the state variable of the system (e.g., the atmospheric temperature), and F is a constant forcing. The model is an autonomous, intrinsically nonlinear, and damped dynamical system under the action of an external forcing.[61] Its properties have been extensively studied, revealing the emergence of chaos when the control parameters, i.e., N_v and F, are varied.[63]

We numerically solve Eq. (29) by employing a fourth-order Runge–Kutta time integration scheme with a time step $\Delta t = 0.05$ corresponding to 6-h resolution in real world time,[61] by using $N_v = 32$ for three different values of the external forcing, $F = 2, 6$, and 10, and running up to $N = 2^{15}$ time points. This allows us to explore different dynamical features of the model,[61,63] passing from a stable non-chaotic steady-state solution characterized by ridging waves at $F = 2$ to a chaotic motion around an unstable equilibrium point when $F = 10$. Figure 8 reports the contours for a subset of time points of the Lorenz '96 model for three different values of the external forcing F, together with the phase-space trajectories of the first two variables x_1 and x_2.

By looking at the phase-space portraits (Fig. 8, bottom panels), we observe that as F increases the dynamics becomes more and more chaotic, as expected, with the Kaplan–Yorke dimension D_{KY} increasing as both N_v and F increase.[63] With the present choice of parameters, it is expected[63] to find $D_{KY} \sim \{1, 14, 20\}$ for $F = \{2, 6, 10\}$ and since D_{KY} is a useful tool to estimate the fractal dimension,[64] we can use these estimates to assess our formalism based on the multiscale generalized fractal dimensions. Figure 9 (left panel) reports the behavior of the multiscale correlation dimension $D_{2,\tau}$ for the three different values of F as an illustrative example, together with the phase-space portraits obtained by using the raw data (gray dots) and the reconstruction of IMFs up to $k = k^*$. Similar findings have also been obtained for $q \neq 2$ (not shown).

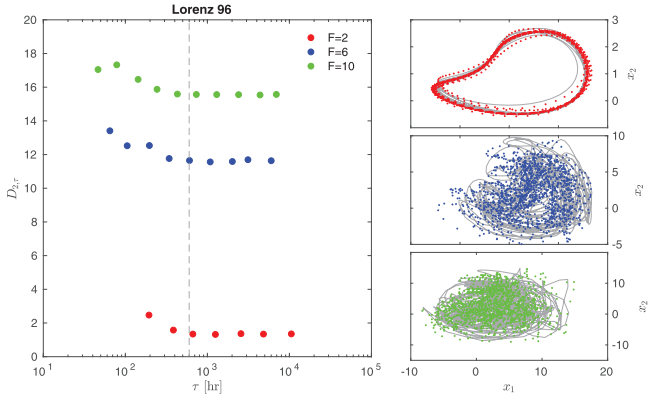

FIG. 9. Left: Behavior of the multiscale correlation dimension $D_{2,\tau}$ vs the timescale τ. The gray dashed line marks the timescale τ^* at which the multiscale correlation dimensions $D_{2,\tau}$ converge to the fractal dimension D_2. Right: Phase-space portraits of the first two variables of the Lorenz '96 model as obtained from the raw time series (x_1, x_2) (gray) and from reconstructions of empirical modes (x_1^*, x_2^*) up to $k^* = 3, 5$, and 6 (red, blue, and green, respectively) for the three different forcing values $F = 2$, 6, and 10 (from top to bottom), respectively.

From Fig. 9, we observe a timescale dependence of the generalized fractal dimensions $D_{q,\tau}$, approaching a constant value for $\tau \gtrsim 600$ h, corresponding to values of $k^* = 3, 5$, and 6 for $F = 2, 6$, and 10 that are lower than the total number of IMFs identified by the procedure ($N_k = 7, 9$, and 11, respectively). As for the previous examples, the convergence to the expected dimensions is observed for $k^* < N_k$, i.e., again only a subset of empirical modes is needed to recover the essential geometric and topological information on the phase-space of the Lorenz '96 model. This can be clearly observed by comparing the phase-space dynamics of the raw data (gray lines) and the reconstruction of IMFs (colored lines) in the (x_1, x_2) phase-space as reported in Fig. 9. We note that the geometric properties of the Lorenz '96 attractor are recovered for each of the different values of F, thus suggesting that we could infer both geometric and topological information about the phase-space trajectories with few "informative" empirical modes. Finally, also the estimated convergence values of the multiscale correlation dimension $D_{2,\tau}$ are compatible with previous estimates of the Kaplan–Yorke dimension D_{KY}, with $D_{2,\tau} \leq D_{KY}$.

F. A higher-dimensional bursting system: The on–off intermittency model

As a final example, we show the results from an on–off intermittency model to investigate how our formalism deals with bursting systems. The studied model has been proposed by Platt *et al.*[65] as a five-dimensional dynamical system describing a process switching abruptly from extended periods of stasis to bursts of large variation, i.e., the so-called on–off intermittency. The model equations read as

$$\dot{x}_1 = x_2, \tag{30}$$

$$\dot{x}_2 = -x_1^3 - 2x_1x_3 + x_1x_5 - \mu_{01}x_2, \tag{31}$$

$$\dot{x}_3 = x_4, \tag{32}$$

$$\dot{x}_4 = -x_3^3 - \nu_{01}x_1^2 + x_3x_5 - \nu_{02}x_4, \tag{33}$$

$$\dot{x}_5 = -\nu_{03}x_5 - \nu_{04}x_1^2 - \nu_{05}\left(x_3^2 - 1\right), \tag{34}$$

where $\mu_{01}, \nu_{01}, \nu_{02}, \nu_{03}, \nu_{04}$, and ν_{05} are the control parameters and the system is inherently nonlinear.[65] The model shows different interesting features, including the existence of a Lorenz '63 like attractor for a particular choice of the control parameters. For the purpose of the present study, we simulate the model dynamics for $N = 2^{14}$ time steps via a Euler scheme with a $\Delta t = 10^{-2}$ and by choosing $\mu_{01} = 1.815$, $\nu_{01} = 1$, $\nu_{02} = 1.815$, $\nu_{03} = 0.44$, $\nu_{04} = 2.86$, and $\nu_{05} = 2.86$.

After having applied the EMD procedure to the time series, we obtained a set of $N_k = 7$ empirical modes that are used to evaluate the multiscale generalized fractal dimensions $D_{q,\tau}$ at different timescales τ. As shown in Fig. 10 (right panel), there is a clear scale-dependent behavior of $D_{q,\tau}$ that tend to converge when $k^* = 6 < N_k$ (although there is still recognizable variation between $k^* = 6$ and $k^* = 7$, the respective values of $D_{q,\tau}$ can be considered similar within their estimated error bounds), thus allowing to reproduce the phase-space dynamics by using a subset of the whole set of empirical modes, as for the previous examples. However, we need to highlight here that the convergence to the expected D_q is obtained by excluding only 1 empirical mode from the whole set of IMFs. Among all dynamical systems studied in the present work, this feature only emerges for this particular example and can be attributed to a key role of bursting in determining the complexity of dynamical systems, together with a remarkable scale-to-scale dependence of geometric and topological properties that is observed up to relatively large timescales. Our approach, therefore, suggests that only a minor complexity reduction can be obtained in terms of empirical modes for such heavily intermittent systems.

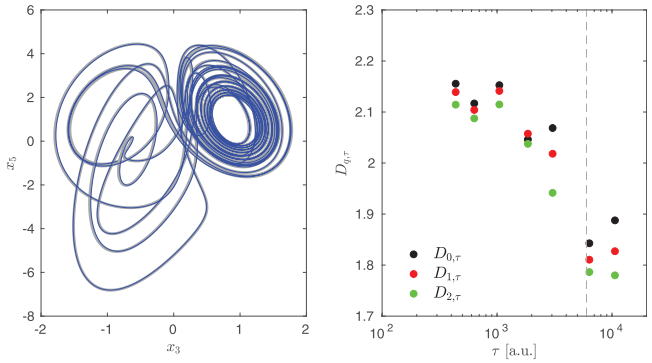

FIG. 10. Left: Phase-space portrait in the (x_3, x_5) plane of the on–off intermittency model as obtained from the raw time series (gray) and from reconstructions of empirical modes up to $k^* = 6$ (blue). Right: Behavior of the multiscale generalized fractal dimensions $D_{q,\tau}$ vs the timescale τ for $q \in [0, 2]$. The gray dashed line marks the timescale τ^* at which the multiscale generalized dimensions $D_{q,\tau}$ converge to the fractal dimensions D_q.

IV. REAL-WORLD APPLICATIONS

Motivated by the successful application of our proposed formalism to a variety of numerical model systems with different types of dynamics (deterministic vs stochastic, time-discrete vs continuous, low-dimensional vs high-dimensional), in the following, we finally discuss two different case studies of real-world signals: the behavior of the global ice volume during the past 5 Myr[39] and the variability of the near-Earth electromagnetic environment as monitored by the SYM-H geomagnetic index.[40] Both time series represent different systems characterized by multiscale physical processes covering a wide range of time scales, allowing us to investigate how our formalism deals with real-world systems by means of two extensively studied examples.[5,43,66–68]

We note that different from the paradigmatic model systems studied above, real-world time series often exhibit not only nonlinear but also nonstationary variability. Strictly speaking, such nonstationarity might not permit the estimation of nonlinear dynamical properties such as the generalized fractal dimensions or at least cast doubts on the proper interpretation of such estimates. Along with applying EMD as a first analysis step, we, however, guarantee here that an essential part of nonstationarity (i.e., slow "drifts" in the mean resulting in monotonic trends or slow variability components) is effectively filtered out by the EMD residual and the slowest oscillatory variability modes, respectively. As a consequence, the reconstructions based on partial sums of intrinsic mode functions representing faster variability components can be expected to exhibit a higher degree of stationarity than the original signals and, therefore, provide interpretable estimates of the generalized fractal dimensions.

As a last preliminary note, we emphasize that the successful application of our formalism to low-to-moderate dimensional paradigmatic model systems alone does not guarantee the applicability to arbitrary real-world time series. The following results shall, therefore, be considered as empirical evidence that the findings to be obtained from such kind of analysis can actually provide meaningful and relevant information on the dynamical characteristics of the system under study. Further bridging the gap between the low-dimensional models (partially being motivated by atmospheric phenomena in the case of the Lorenz '83 and '96 models) and the real-world observational time series in terms of additional analyses of the dynamics of more complex models of paleoclimate and geomagnetic variability, respectively, will be a subject of future research.

A. LR04 paleoclimate record

As a first example, we consider the investigation of paleoclimate changes on different timescales. As also reported in several previous works (e.g., Refs. [66–68]), the history of the Earth's climate variability comprises periods in which global temperatures increased/decreased in a relatively regular oscillatory manner, whose variability changed during the so-called Mid-Pleistocene Transition (MPT), characterized by a pronounced 41-kyr (thousands of years) timescale before 1200 kyr BP and a different dynamical regime, in which oscillations on an about 100-kyr timescale dominate during the last 700 kyr.[66] Several attempts have been made to characterize this transition, mostly dealing with the idea of the occurrence of a bifurcation on a slow manifold.[66,68] Here, we test if our formalism can help characterizing the dynamical changes at different scales by looking for dimensionality reductions and/or bifurcations between different climate states.

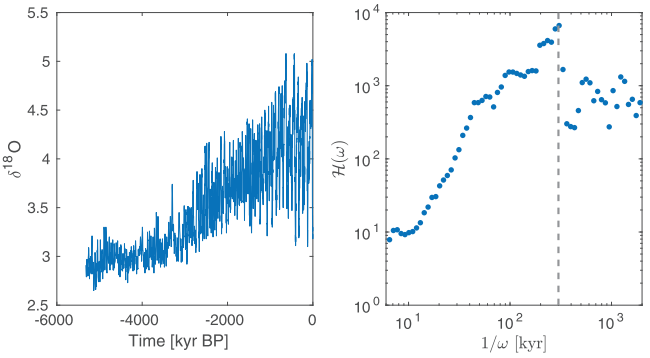

FIG. 11. Left: Time series of the δ^{18}O stack record during the last 5.3 Myr. Right: Hilbert marginal spectrum $H(\omega)$ shown as a function of $1/\omega$.

For this purpose, we use the LR04 time series (consisting of $N = 2115$ data points), which has been constructed by stacking oxygen isotope ratio (δ^{18}O) data measured on benthic foraminifera from 57 globally distributed deep sea sediment cores (see Fig. 11, left panel) and is considered a combined proxy for the global ice volume and the deep ocean temperature during the past 5.3 Myr (millions of years).[39] This record has been tuned to an orbitally driven ice sheet model in which changes in the 65°N summer solstice insolation due to long-term variations in the Earth's orbital parameters are assumed to be the cause of variations of the global ice volume on orbital scales. We note that the LR04 time series has a non-uniform sampling, spanning from $\Delta t = 1$ kyr up to $\Delta t = 5$ kyr. Although it has no direct effect on the EMD procedure,[38] this non-uniform sampling could slightly affect the estimation of the fractal dimensions via the time-delay embedding procedure proposed by Takens.[69] Since the present work is not devoted on the comparison between existing phase-space reconstruction methods, we will not go deeper into typical problems affecting the time-delay embedding estimations. The reader is referred to Lekscha and Donner[69] for a detailed investigation of the performance of differential and time-delay embedding methods.

Applying EMD to the LR04 record, a set of $N_k = 11$ empirical modes has been obtained, which capture variability on timescales from $\tau_1 \sim 7$ kyr up to $\tau_{11} \sim 1.6$ Myr. By looking at the global energy distribution as measured by the Hilbert marginal spectrum $H(\omega)$, we find evidence for three different regimes corresponding to $1/\omega \lesssim 10$ kyr, 10 kyr $\lesssim 1/\omega \lesssim 300$ kyr, and $1/\omega \gtrsim 300$ kyr, respectively (see Fig. 11, right panel).

Next, we evaluate the multiscale generalized fractal dimensions $D_{q,\tau}$ at different timescales τ, whose behavior is clearly timescale-dependent with some interesting features, as shown in Fig. 12. $D_{q,\tau}$ have been evaluated by time-delay embedding of each IMF with $m = 3$, but different embedding delays Δ_k corresponding to the first minimum of the time-delayed average mutual information function of each respective mode. The choice of $m = 3$ provides a balance

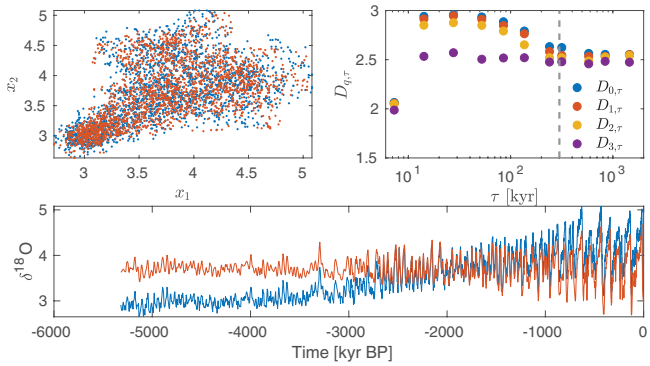

FIG. 12. Top left: Phase-space portrait of the two first embedding components of the LR04 record as obtained by the raw data (blue) and by empirical mode reconstructions (orange) with $k^* \in [2, 7]$. Top right: Behavior of the multiscale generalized fractal dimensions $D_{q,\tau}$ vs the timescale τ for $q \in [0, 3]$. The gray dashed line marks the timescale τ^* at which the multiscale generalized dimensions $D_{q,\tau}$ converge to a constant value D_q. Bottom: Time evolution of the δ^{18}O stack record during the last 5.3 Myr (blue) and reconstructions of empirical modes (orange) with $k^* \in [2, 7]$.

between the high-dimensional nature of the paleoclimate variability (especially on short timescales) and the observation that statistics can only be expected to provide qualitatively robust estimates up to $m = m_{\max}$ depending on the number of available embedding vectors.

First of all, by considering $k^* = 1$ all D_{q,τ_1} assume the same value close to 2, which is in agreement with the fact that when investigating real-world signals, the first IMF could be associated to the noise content of the time series, which is also supported by the flat spectrum observed for $1/\omega \lesssim 10$ kyr. A similar behavior characterized by multiscale generalized fractal dimensions approaching a constant value is observed for $1/\omega \gtrsim 300$ kyr as well, with also $D_{q,\tau>\tau_7}$ being characterized by similar values for all q. Thus, this suggests (to good approximation) that a monofractal character is recovered at large timescales, also well in agreement with the flat spectrum observed in the right panel of Fig. 11, as well as with previous findings.[2] However, the most interesting behavior is found for the intermediate range of timescales, where a clear τ- and q-dependent behavior is found for $D_{q,\tau}$, approaching a constant value when $k^* = 7$. This suggests that the intermediate range of timescales is characterized by multifractal features that are scale-dependent, approaching a monofractal when large-scale components are considered. In a similar way as for the dynamical systems examples discussed in Sec. III, we reconstruct empirical modes up to the mode number $k^* = 7$ as

$$F_7^{(\delta^{18}O)}(t) = \delta^{18}O^*(t) = \sum_{k=2}^{7} c_k^{(\delta^{18}O)}(t), \tag{35}$$

and investigate the dynamical behavior in phase-space by using time-delay embedding with $m = 3$ and the embedding delay corresponding to the recommended value for the complete reconstructed series according to the mutual information criterion. By comparing both the phase-space portrait of the embedded LR04 record [Fig. 12 (upper left panel)] and the time behavior [Fig. 12 (lower panel)] obtained from the raw data with those resulting from reconstructions based on intrinsic mode functions, we note a generally good agreement (except for the missing low-frequency variability in the reconstruction), thus underlining that the essential topological properties of the phase-space can also here be inferred from a few "informative" empirical modes, which correspond to the intermediate range of timescales, e.g., 10 kyr $\lesssim 1/\omega \lesssim$ 300 kyr, closely associated with the Milankovitch scales (i.e., persistent periodic components of the Earth's orbital parameters that are responsible for long-term variations of the spatiotemporal distribution of solar insolation at the Earth's surface).

Moreover, it seems that a different degree of complexity is found when different components are considered. Specifically, we note that the maximum values of $D_{q,\tau}$ correspond to taking into account dynamical components up to ∼40 kyr, while additional large-scale empirical modes tend to reduce the values of the multiscale generalized fractal dimensions. This suggests that the different scale-dependent fluctuations play different roles in determining the topological properties of the system, passing from a (slightly) higher to a (slightly) lower dimensional chaotic dynamics.

B. SYM-H geomagnetic variability index

Another interesting real-world application of our formalism is the comprehension of the dynamical behavior of the Earth's magnetosphere. As recently shown,[5] the forecast horizon of the dynamical state of the magnetosphere significantly changes when different timescales are considered, reflecting the different processes determining the internal dynamics of the magnetosphere.[70] This leads to serious challenges to the forecasting and modeling of space weather phenomena, highly affecting our technological society.

In order to investigate the suitability of our formalism in the framework of space weather, we use the SYM-H geomagnetic index, a proxy for the dynamical state of the magnetospheric activity.[40] More specifically, we consider 5-min time resolution data covering the period between August 24 and September 1, 2018 ($N = 2304$ data points with uniform spacing), which is characterized by the occurrence of a geomagnetic storm, i.e., a decrease of the SYM-H index to strongly negative values, which is a reflection of enhanced activity of the magnetospheric electrical ring current due to the solar wind variability.[70]

As shown in Fig. 13 (left panel), the SYM-H index variability has been initially characterized by values close to 0 nT, before a sudden decrease is observed, corresponding to the main phase of the geomagnetic storm that occurred on August 26, the strongest storm of the year 2018. Then, a long-lasting recovery phase is observed until the SYM-H index moves toward normal quiet-time values. By applying EMD, we derive a set of $N_k = 9$ empirical modes, whose timescales range from $\tau_1 \approx 15$ min up to $\tau_9 \approx 3$ days, and by looking at the behavior of the Hilbert marginal spectrum $H(\omega)$, we note the existence of a spectral scale break at $1/\omega_b \sim 300$ min[71] (see Fig. 13, right panel). Then, we apply our formalism to the derived set of IMFs by evaluating the multiscale generalized fractal dimensions, via time-delay embedding with an embedding dimension of $m = 3$ and different embedding delays corresponding again to the first

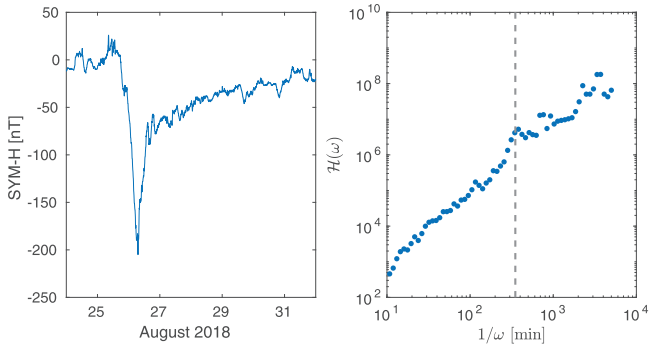

FIG. 13. Left: Time series of the SYM-H index between August 24 and September 1, 2018. Right: Hilbert marginal spectrum $H(\omega)$ shown as function of $1/\omega$.

minimum of the average time-delayed mutual information function, as reported in Fig. 14 (upper right) as a function of the mean timescale τ.

We clearly note that there exists a timescale separation, exactly matching the spectral separation obtained by the Hilbert spectral analysis, which is a reflection of the different processes characterizing the dynamical state of the Earth's magnetosphere. Again, the first IMF appears associated with the noise content of the time series or the digitization process in deriving the SYM-H index from geomagnetic field measurements.[5,40,71] Then, $D_{q,\tau}$ are characterized by a multifractal behavior, spanning a wide range of values when both q and τ are varied. Moreover, it is interesting to note that they approach constant values when $\tau > 300$ min, ranging between

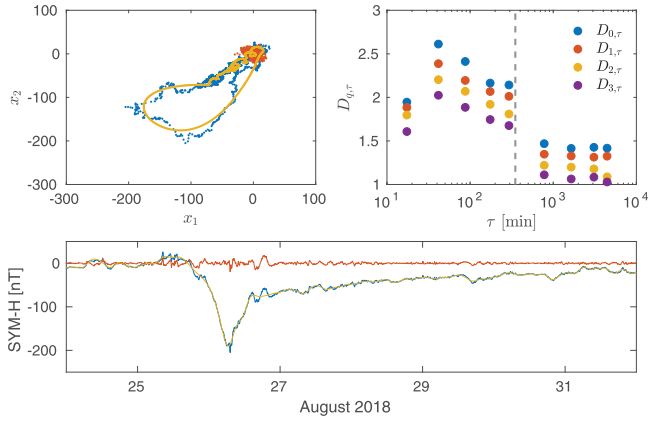

FIG. 14. Top left: Phase-space portrait of the SYM-H index variability as obtained by the raw data (blue), by empirical mode reconstructions (orange) with $k^* \in [2, 5]$ (fast dynamics), and by empirical mode reconstructions (yellow) with $k^* \in [6, 9]$ (slow dynamics). Top right: Behavior of the multiscale generalized fractal dimensions $D_{q,\tau}$ vs the timescale τ for $q \in [0, 3]$. The gray dashed line marks the timescale τ^* at which the multiscale generalized dimensions $D_{q,\tau}$ converge to a constant value D_q. Bottom: Time series of the SYM-H index (blue), fast (orange) and slow (yellow) dynamical components as obtained by reconstructing empirical modes with $k^* \in [2, 5]$ and $k^* \in [6, 9]$, respectively.

$D_{3,\tau>300\,\mathrm{min}} \approx 1$ and $D_{0,\tau>300\,\mathrm{min}} \approx 1.5$. This seems to suggest that a more regular behavior is found at these timescales, which can be directly related to the solar wind variability and to the nonlinear response of the magnetosphere to solar wind changes.[70,71] Indeed, the resulting separation between fast and slow dynamical components is the reflection of the different origins of both components: the fast dynamics is related to the internal dynamics of the magnetosphere, mostly associated with processes taking place in the so-called magnetotail,[5,70] which are triggered by the changes of the interplanetary conditions, while the slow dynamics is mainly directly driven by the solar wind changes, being mainly related to the enhancement of the large-scale magnetospheric convection process.[70]

This separation seems to be also highlighted by our formalism, which additionally allows us to interpret it in a dynamical system framework. First, we need to underline that reconstructing the phase-space trajectory by using the raw data allows us to evidence the existence of two different phase-space regions: one corresponds to the quiet-time values of the SYM-H index and the other to the disturbed-time ones [see blue points in Fig. 14 (upper left)]. Interestingly, when reconstructing the phase-space dynamics by using empirical mode reconstructions with $k^* \in [2, 5]$ [orange points in Fig. 14 (upper left)] we note that it does not quite reproduce the phase-space dynamics of the SYM-H index variability as obtained by the raw data [blue points in Fig. 14 (upper left)]. This suggests that some relevant information is missed in the reconstruction and hence must be stored in the remaining empirical modes. Motivated by those findings, we finally provide reconstructions of IMFs on large timescales (e.g., $k^* \in [6, 9]$) and investigate the phase-space dynamics associated with this component [yellow points in Fig. 14 (upper left)]. The resulting reconstruction indeed covers those phase-space regions, which have not been captured by the fast component. This can be interpreted as a signature of the existence of a different origin of processes operating on short and long timescales, thus not allowing us to reproduce the phase-space dynamics with few empirical modes but requiring the consideration of a larger set of "informative" IMFs, being characterized by completely different multiscale measures, i.e., a more chaotic (less predictable) behavior for the fast component (higher $D_{q,\tau<300\,\mathrm{min}}$) and a more regular (more predictable) dynamics of the slow component (lower $D_{q,\tau>300\,\mathrm{min}}$). These findings completely agree with previous works,[5,70] where a timescale separation has been found for correctly characterizing the dynamical state of the Earth's magnetosphere.

V. DISCUSSION AND CONCLUSIONS

In this paper, we have introduced a new formalism in which empirical mode decomposition is first used to detect embedded oscillations inside signals, before the complexity and topology of variability components iteratively reconstructed from those oscillatory modes are investigated by using the generalized fractal dimension approach.[12] The results obtained for pedagogical low- and high-dimensional deterministic examples like the Hénon map, the Lorenz '63 system, the standard map, the Lorenz '96 model, and the on–off intermittency model, as well as stochastic processes from the family of fractional Brownian motions point toward great potentials of this approach for exploiting the information content of fluctuations at different scales.

While the studied numerical examples provide a selection of common types of dynamics, we are aware of the fact that they necessarily do not provide a fully exhaustive sample. On the one hand, we have focused on systems with different kinds of multiscale variability, thereby leaving models exhibiting single-scale dynamics (like periodic or narrow-band chaotic oscillations) aside since those would be trivially captured by single, or at most very few, intrinsic mode functions. Similar considerations do apply to simple slow–fast dynamical systems, which have also been studied in the course of this work (results not shown). On the other hand, extensions to high-dimensional chaotic systems like space–time chaotic dynamics or sophisticated models of climate or geomagnetic variability considered here as real-world examples would be possible (and are already partly under investigation), yet in our opinion deserve more explicit analysis and separate reporting beyond the limitations of the present work.

Based on the variety of model systems of different nature and properties studied in this work, our formalism reveals that for a signal $\{x_i\}_{i=1}^{N}$ comprised by N_k modes of fluctuations on different scales τ_k, its trajectories can be typically described, in terms of information content, by a subset of modes of size $N_{k^*} < N_k$. It is striking to note that it is always the slowest modes that do not contribute to the phase-space trajectory reconstructions. However, this feature cannot be solely attributed to the time series length. Indeed, in our corresponding analysis of the Hénon map, we noted that the convergence toward the expected dimensions occurred always at the same timescale even when the length of time series is increased from $N = 2^{11}$ to $N = 2^{15}$. This observation indicated that our formalism could also be helpful to infer the necessary time series length for capturing the essential dynamics of the system.

We, therefore, suggest that our formalism can open new perspectives for the investigation and characterization of the dynamical properties of physical systems in which a multiscale behavior is observed, being also characterized by a different nature of the processes involved. Indeed, this formalism allowed us to investigate the existence of a timescale separation between processes of different origin characterizing the near-Earth electromagnetic environment as monitored by the SYM-H index. We have shown how the proposed formalism well reproduced the phase-space dynamics by selecting the "more informative" IMFs within the whole set extracted from the EMD algorithm.

Moreover, our formalism also allows us to investigate how the degree of complexity changes when different components (e.g., timescales) are considered. This is well explained by looking at the results we obtained in the framework of paleoclimate variability, where maximum values of $D_{q,\tau}$ correspond to take into account dynamical components up to $\sim$40 kyr, while additional large-scale empirical modes tend to reduce the values of the multiscale generalized fractal dimensions, until the passage from a multifractal to a monofractal behavior is observed at larger scales $\tau \gtrsim 300$ kyr. This suggests that the different scale-dependent fluctuations play different roles in determining the topological properties of the system.

We need to highlight that there exist other EMD-based methods that have been previously used along with dynamical complexity measures similar as in the present work, yet with distinctive differences. Sharma *et al.*[72] proposed a method for the classification of electroencephalogram signals by first decomposing the time series into empirical modes and then computing entropy measures (like the Shannon entropy or average Rényi entropy) for each empirical mode individually. Liaw and Chiu[73] introduced a procedure for studying crossover-fractals, which uses the EMD to first decompose monofractal signals and then employs partial sums of the empirical modes to construct crossover-fractals via the evaluation of scale-dependent fractal dimensions. However, our formalism differs from those previously proposed methods, since it is based on evaluating the generalized fractal dimensions directly from iterative reconstructions based on empirical modes instead of evaluating complexity and/or entropy measures of the different IMFs. In this way, our approach directly allows us to investigate how the different empirical modes contribute to the geometric and topological information stored in the original time series and to control the obtained results, since due to the completeness property of the EMD the multiscale dimensions necessarily converge toward the expected fractal dimensions of the time series.

It should be further noted, that a similar formalism can be constructed by replacing the EMD with a different time series decomposition technique (like discrete wavelet decomposition, dynamic mode decomposition, or others). In this context, we would like to recall that the idea of time series decomposition implies an additive superposition of modes. From this perspective, all such decomposition methods are linear, as the original data are interpreted as a sum of components with different typical time scales. At present, we are not aware of any established strictly nonlinear time series decomposition method, i.e., some data analysis technique that allows us to write the raw data as a nonlinear (non-additive) combination of individual components. The key point underlying existing decomposition techniques is that an n-dimensional (continuous, for notation simplicity) nonlinear system can be described as

$$\dot{x}_i = F_i(x_j, \{\beta\}) \quad \text{with} \quad i, j = 1, \ldots, n, \tag{36}$$

where nonlinearities are embedded into the dependence of F_i on the system variables in a nonlinear way, e.g.,

$$F_i(x_j, \mu_i) = \sum_{i,j} \mu_j x_j^{\alpha_j} + \eta_{ij} x_i^{\gamma_i} x_j^{\delta_j}, \tag{37}$$

with $\{\beta\} = \{\mu_i, \eta_{ij}, \alpha_i, \gamma_i, \delta_i\}$ being the set of control parameters. Dealing with time series measurements of the system variables, i.e., $x_i(t)$, we are not able to appreciate the "explicit" nonlinear dependence on variables but we can only account for the "implicit" nonlinear dependence on time. Nevertheless, we emphasize that despite their conceptual limitations as discussed above, such linear time scale decomposition methods have been successfully applied in past research to identify the dynamical backbone of complex nonlinear dynamics. One prominent example is the observation that the emergence of synchronization processes between coupled chaotic systems is an intimately timescale-dependent process[74–77] that can be efficiently studied by means of wavelet decomposition. A similar wavelet based technique has been suggested by Palus[78,79] for analyzing coupling and causality patterns among phase and amplitude variables characterizing variability at different time scales.

The above considerations are especially valid for univariate data, where a single representative dependent variable of the dynamics (e.g., the SYM-H index) is investigated as a function of a single dependent variable (time). However, within the very wide range of data analysis methods currently implemented, there are a few really promising cases in terms of their local and adaptive nature as well as their suitability for dealing with nonlinear dynamical and real-world systems. One of these is surely the EMD that could be more convenient than some of those other methods with more *a priori* constraints and reduce possible artifacts, e.g., due to a fixed-frequency decomposition basis. Moreover, the time-dependency of the amplitudes of empirical modes allows us a more detailed investigation of the dynamical evolution (in time) of a system variable, following its local (in terms of time) variations[38] as compared to fixed-amplitude methods.

In summary, we are confident that the formalism proposed here can be generally helpful to investigate the role of multiscale fluctuations within complex systems, allowing us to retain and identify empirical modes storing more information within the whole set of scales as well as to deal with the problem of characterizing the role of stochastic fluctuations in several physical systems.[1,2,35,80,81] Furthermore, a similar formalism can be easily built up for other complexity and/or entropy measures, instead of evaluating fractal properties in terms of generalized dimensions. Investigating all these aspects in more detail is beyond the scope of the present paper and will be the subject of future work.

ACKNOWLEDGMENTS

The authors acknowledge the World Data Center for Geomagnetism (Kyoto) for making the geomagnetic indices data publicly available. T.A. acknowledges the Institute for Space Astrophysics and Planetology (IAPS) for its support within the framework "Bando Nuove Idee IAPS 2019." G.C. acknowledges financial support by the Italian MIUR-PRIN (Grant No. 2017APKP7T) on Circumterrestrial Environment: Impact of Sun-Earth Interaction. P.D.D. received funding from the H2020 Project TiPES (No. 820970). R.V.D. has received partial support from the German Federal Ministry for Education and Research (BMBF) via the Young Investigators Group CoSy-CC^2 (Grant No. 01LN1306A) and the JPI Climate/JPI Oceans project ROADMAP (Grant No. 01LP2002B). V.Q. acknowledges the Italian Space Agency for financial support under the Contract ASI "LIMADOU scienza" (No. 2016-16-H0). T.A., G.C., and R.V.D. acknowledge fruitful discussions within the scope of the International Team "Complex Systems Perspectives Pertaining to the Research of the Near-Earth Electromagnetic Environment" at the International Space Science Institute in Bern, Switzerland. The authors thank two anonymous reviewers for fruitful suggestions.

DATA AVAILABILITY

The data that support the findings of this study are available from the corresponding author upon reasonable request. The LR04 stack data are openly available, at https://lorraine-lisiecki.com/stack.html, Ref. 39 and the OMNI data in GSFC/SPDF OMNIWeb interface at https://omniweb.gsfc.nasa.gov/, Ref. 83.

REFERENCES

[1] S. Lovejoy and D. Schertzer, *The Weather and Climate: Emergent Laws and Multifractal Cascades* (Cambridge University Press, Cambridge, 2013), p. 475.
[2] Z.-G. Shao and P. D. Ditlevsen, Nat. Commun. **7**, 10951 (2016).
[3] U. Frisch, *Turbulence. The Legacy of A. N. Kolmogorov* (Cambridge University Press, Cambridge, 1995), p. 296.
[4] R. Bruno and V. Carbone, *Turbulence in the Solar Wind* (Springer, Heidelberg, 2016), p. 267.
[5] G. Consolini, T. Alberti, and P. De Michelis, J. Geophys. Res. **123**, 9065, https://doi.org/10.1029/2018JA025952 (2018).
[6] P. Grassberger, T. Schreiber, and C. Schaffrath, Int. J. Bifurc. Chaos **01**, 521–547 (1991).
[7] S. M. Pincus, Proc. Natl. Acad. Sci. U.S.A. **88**, 2297–2301 (1991).
[8] M. Costa, A. L. Goldberger, and C.-K. Peng, Phys. Rev. Lett. **89**, 062102 (2002).
[9] B. B. Mandelbrot, *The Fractal Geometry of Nature* (Freeman, San Francisco, 1982), p. 468.
[10] R. V. Donner, J. Heitzig, J. F. Donges, Y. Zou, N. Marwan, and J. Kurths, Eur. Phys. J. B **84**, 653–627 (2011).
[11] H. G. E. Hentschel and I. Procaccia, Physica D **8**, 435 (1983).
[12] P. Grassberger and I. Procaccia, Phys. Rev. Lett. **50**, 346 (1983).
[13] T. C. Halsey, M. H. Jensen, L. P. Kadanoff, and I. Procaccia, Phys. Rev. A **33**, 1141 (1986).
[14] G. Parisi and U. Frisch, in *Proceedings of the International School on Turbulence and Predictability in Geophysical Fluid Dynamics and Climate Dynamics* (North-Holland, Amsterdam, 1985), p. 84.
[15] D. Harte, *Multifractals. Theory and Applications* (Chapman & Hall, London, 2001), p. 264.
[16] F. Anselmet, Y. Gagne, E. J. Hopfinger, and R. A. Antonia, J. Fluid Mech. **140**, 63 (1984).
[17] B. Castaing, Y. Gagne, and E. J. Hopfinger, Physica D **46**, 177 (1990).
[18] E. Marsch and S. Liu, Ann. Geophys. **11**, 227 (1993).
[19] L. Sorriso-Valvo, V. Carbone, P. Veltri, G. Consolini, and R. Bruno, Geophys. Res. Lett. **26**, 1801, https://doi.org/10.1029/1999GL900270 (1999).
[20] V. Carbone, R. Marino, L. Sorriso-Valvo, A. Noullez, and R. Bruno, Phys. Rev. Lett. **103**, 061102 (2009).
[21] T. Alberti, G. Consolini, V. Carbone, E. Yordanova, M. F. Marcucci, and P. De Michelis, Entropy **21**, 320 (2019).
[22] C. Meneveau and K. R. Sreenivasan, Phys. Lett. A **137**, 103 (1989).
[23] D. V. Vassiliadis, A. S. Sharma, T. E. Eastman, and K. Papadopoulos, Geophys. Res. Lett. **17**, 1841, https://doi.org/10.1029/GL017i011p01841 (1990).
[24] G. Consolini, M. F. Marcucci, and M. Candidi, Phys. Rev. Lett. **76**, 4082 (1996).
[25] C. E. Shannon, Bell Syst. Tech. J. **27**, 379 (1948).
[26] M. Palus, Phys. Lett. A **213**, 138 (1996).
[27] T. Schreiber, Phys. Rev. Lett. **85**, 461 (2000).
[28] M. Palus, A. Krakovská, J. Jakubík, and M. Chvosteková, Chaos **28**, 075307 (2018).
[29] H. Kantz and T. Schreiber, *Nonlinear Time Series Analysis* (Cambridge University Press, Cambridge, 2004), p. 388.
[30] H. A. Dijkstra, *Nonlinear Climate Dynamics* (Cambridge University Press, Cambridge, 2013).
[31] E. N. Lorenz, J. Atmos. Sci. **20**, 130 (1963).
[32] G. Gallavotti, *Statistical Mechanics. A Short Treatise* (Springer-Verlag, Berlin, 2000), p. 354.
[33] A. Einstein, Ann. Phys. **17**, 549 (1905).
[34] P. Langevin, C.R. Acad. Sci. Paris **146**, 530 (1908).
[35] L. F. Richardson, *Weather Prediction by Numerical Process* (Cambridge University Press, Cambridge, 2007), p. 250.
[36] S. B. Pope, *Turbulent Flows* (Cambridge University Press, Cambridge, 2000), p. 771.
[37] A. N. Kolmogorov, Dokl. Akad. Nauk SSSR **30**, 301 (1941).
[38] N. E. Huang *et al.*, Proc. R. Soc. London Ser. A **454**, 903 (1998).
[39] L. E. Lisiecki and M. E. Raymo, Paleoceanography **20**, 437 (2005).
[40] T. Iyemori, J. Geomagn. Geoelectr. **42**, 1249 (1990).
[41] P. Flandrin, G. Rilling, and P. Goncalves, IEEE Signal Process. Lett. **11**, 2 (2004).

[42]G. Rilling, P. Flandrin, and P. Goncalves, in *Proceedings of the IEEE-EURASIP, Workshop on Nonlinear Signal and Image Processing NSIP-03, Grado, Italy* (IEEE, 2003).
[43]T. Alberti, Il Nuovo Cimento **41C**, 113 (2018).
[44]G. Consolini *et al.*, J. Phys. Conf. Ser. **900**, 012003 (2017).
[45]J. G. Reid and T. A. Trainor, "Correlation analysis with scale-local entropy measures," arXiv:math-ph/0304010 (2003a).
[46]J. G. Reid and T. A. Trainor, "Scale-local dimensions of strange attractors," arXiv:math-ph/0305022 (2003b).
[47]P. Grassberger, Phys. Lett. A **107**, 101 (1985).
[48]M. Henon, Comm. Math. Phys. **50**, 69 (1976).
[49]R. A. da Costa and M. Eisencraft, in *Proceedings of the 8th International Conference on Nonlinear Science and Complexity* (SWGE Sistemas, 2016), Vol. 42.
[50]F. Takens, "Detecting strange attractors in turbulence," in *Dynamical Systems and Turbulence*, Lecture Notes in Mathematics, edited by D. A. Rand and L.-S. Young (Springer-Verlag, 1981), Vol. 898, pp. 366–381.
[51]Z. Ming-Wei, F. Guo-Lin, and G. Xin-Quan, Chin. Phys. **15**, 1384 (2006).
[52]J. Argyris, I. Andreadis, G. Pavlos, and M. Athanasiou, Chaos Soliton. Fract. **9**, 343 (1998).
[53]Z. Wu and N. E. Huang, Proc. R. Soc. London A **460**, 1597 (2004).
[54]D. Farmer, J. Crutchfield, H. Froehling, N. Packard, and R. Shaw, Ann. New York Acad. Sci. **357**, 453 (1980).
[55]E.-H. Park, M.-A. Zaks, and J. Kurths, Phys. Rev. E **60**, 6627 (1999).
[56]V. Lucarini, J. Stat. Phys. **134**, 381 (2009).
[57]P. Cvitanovic, M. H. Jensen, L. P. Kadanoff, and I. Procaccia, Phys. Rev. Lett. **55**, 343 (1985).
[58]G. Voyatzis, "Low frequency power spectra and classification of Hamiltonian trajectories," in *Galaxies and Chaos*, Lecture Notes in Physics (Springer, 2003), Vol 626, pp. 126–136.
[59]Y. Zou, R. V. Donner, M. Thiel, and J. Kurths, Chaos **26**, 023120 (2016).
[60]M. Harsoula, K. Karamanos, and G. Contopoulos, Phys. Rev. E **99**, 032203 (2019).
[61]E. N. Lorenz, Proc. Seminar Predict. **1**, 1 (1996).
[62]E. N. Lorenz and K. A. Emanuel, J. Atmos. Sci. **655**, 399 (1998).
[63]A. Karimi and M. L. Paul, Chaos **20**, 043105 (2010).
[64]J. L. Kaplan and J. A. Yorke, "Chaotic behavior of multidimensional difference equations," in *Functional Differential Equations and Approximation of Fixed Points*, Lecture Notes in Mathematics, edited by H. O. Peitgen and H. O. Walther (Springer, Berlin), Vol. 730.
[65]N. Platt, E. A. Spiegel, and C. Tresser, Phys. Rev. Lett. **70**, 279 (1993).
[66]P. D. Ditlevsen and P. Ashwin, Front. Phys. **6**, 62 (2018).
[67]M. Crucifix, Philos. Trans. R. Soc. A **370**, 1140 (2012).
[68]I. Daruka and P. D. Ditlevsen, Clim. Dyn. **46**, 29 (2016).
[69]J. Lekscha and R. V. Donner, Chaos **28**, 085702 (2018).
[70]T. Alberti, G. Consolini, P. De Michelis, M. Laurenza, and M. F. Marcucci, J. Space Weather Space Clim. **8**, A56 (2018).
[71]B. Tsurutani, M. Sugiura, T. Iyemori, B. E. Goldstein, W. D. Gonzalez, S.-I. Akasofu, and E. J. Smith, Geophys. Res. Lett. **17**, 279–282, https://doi.org/10.1029/GL017i003p00279 (1990).
[72]R. Sharma, R. B. Pachori, and U. R. Acharya, Entropy **17**, 669 (2015).
[73]S.-S. Laiw and F.-Y. Chiu, Adv. Adapt. Data Anal. **2**, 509 (2010).
[74]A. E. Hramov and A. A. Koronovskii, Chaos **14**, 603 (2004).
[75]A. A. Koronovskii and A. E. Hramov, Techn. Phys. Lett. **30**, 29 (2004).
[76]R. Donner, "Phase coherence analysis of decadal-scale sunspot activity on both solar hemispheres," in *Nonlinear Time Series Analysis in the Geosciences*, Lecture Notes in Earth Sciences, edited by R. V. Donner and S. M. Barbosa (Springer, 2008), Vol. 112, pp. 355–385.
[77]S. Gupta, S. De, M. S. Janaki, and A. N. Sekar Iyengar, Phys. Rev. E **100**, 022218 (2019).
[78]M. Palus, Phys. Rev. Lett. **112**, 078702 (2014).
[79]M. Palus, Entropy **16**, 5263 (2014).
[80]T. Alberti, G. Consolini, and V. Carbone, Chaos **29**, 103107 (2019).
[81]S. Lovejoy, Nonlin. Process. Geophys. Discuss. (published online).
[82]N. Rehman and D. P. Mandic, Proc. R. Soc. A **466**, 1291 (2010).
[83]See https://omniweb.gsfc.nasa.gov/ for OMNI data in GSFC/SPDF OMNIWeb interface.